A projection way for constructing the WENO limiter for discontinuous Galerkin spectral element method

Wanai Li[a,*], Yu-Xin Ren[b]
Corresponding author: (*) liwai@mail.sysu.edu.cn

[a] Sino-French Institute of Nuclear Engineering and Technology, Sun Yat-Sen university, ZhuHai, China.
[b] Department of Engineering Mechanics, Tsinghua university, Beijing, China.

Abstract

This paper proposes a projection-WENO limiter for discontinuous Galerkin spectral element method on unstructured quadrilateral grids. This limiter can keep high order accuracy in smooth regions and suppress numerical oscillations efficiently near discontinuities. The WENO scheme proposed in the present paper is the wighted average of the high order polynomial in the central cell and the linear polynomials constructed through a L_2 projection in the central and face-neighboring cells. The WENO smooth indicator is modified by the introduction of a small ε which is related to the discontinuity strength to achieve better shock capturing. A number of compressible flow cases are calculated to demonstrate the high order accuracy and non-oscillation properties of the constructed limiter.

Keywords: Numerical Algorithms, Computational Fluid Dynamics, Turbulence Modeling, Aeroacoustics.

1 Introduction

The discontinuous Galerkin spectral element method (DGSEM), as a nodal-type discontinuous Galerkin (DG) method, has shown great convenience and efficiency in solving the convection-diffusion equation [1] on tensor-product grids. The approximate solution uses the tensor-product Lagrange interpolation polynomial associated with Gauss-Legendre quadrature points. The collated interpolation and quadrature points give higher efficiency comparing with the standard modal type DG method. The implicit time integration based on a matrix-free Newton-Krylov-Schwarz algorithm was used to accelerate the convergence speed for the DGSEM scheme [2]. Applications of DGSEM widely spread over multi-phase flows [3], transitional and turbulent flows [4, 5].

The presence of shock waves in the compressible flow requires special treatments in the DG method. The inner degrees of freedom (DOF) in the DG approximate solution would induce large numerical oscillations near the discontinuities. An accuracy-preserving and oscillation-free approach for shock capturing is still one of the most challenging issues for the DG method. The slope limiting technique is a popular way in the finite volume (FV) method [6, 7] and brought into the DG method for its simplicity [8]. The robustness of this method strongly relies on the underlying criteria for singling out the troubled cells. A comparison is given on a second-order slope limiter based on the TVB detector [9] and the Fu-Shu detector [10]. The TVB detector gave smooth results with low resolutions for the strong shock problems, while the Fu-Shu detector gave higher resolution results with some numerical oscillations in the smooth regions. The shock detector usually mistook the smooth cell near extremas for the troubled cell and the accuracy was degraded with a second-order slope limiter. High order limiting ways are pursued to relieve the difficulty of designing the shock detectors and to improve the resolution near discontinuities. The multi-dimensional optimal order (MOOD) approach in the finite volume method [11] was introduced in the DG method by Dumbser et al [12] and Sonntag et al [13]. The sub-cell division combining with a TVD-type slope limiter in MOOD preserved the accuracy of the DG method in smooth regions. The WENO limiter achieved great success in finite difference (FD) and FV methods, and was also applied in the DG methods. The FV type WENO limiter was first introduced by Zhu et al [14] on unstructured grids. The Hermite WENO [15] and secondary-reconstruction based WENO [16] limiters were proposed to fully utilize all the inner DOFs in the DG method.

The problem of the WENO approaches is that the construction is complicated and their sub-cell shock capturing abilities are still far from satisfied.

In reference [17], the DGSEM was generalized to triangular grids and a high-resolution second-order WENO limiter was developed on 2D mixed grids. This paper proposes a high order compact projection-WENO limiter for DGSEM on quadrilateral grids. The projection-WENO limiter would be different from the current WENO limiters [14, 15, 16]. The candidate polynomials in the projection-WENO limiter contain the high order one in the central cell and several linear ones, which are constructed through the L_2 projection in the central and face-neighboring cells. The construction of linear polynomials brings the possibility to remove numerical oscillations in inner DOFs near strong shocks. The scheme's accuracy is guaranteed by the WENO weighted summation of all the candidate polynomials. The implementation on 2D quadrilateral grids fully utilizes the tensor-product structure of the approximation solution in DGSEM. The limiting would be proceeded dimension by dimension to save computational cost. For the nonlinear Euler equations, the way in [16] is adopted to perform the limiting in the characteristic space. Our purpose is to design a realizable limiter on general quadrilateral grids which can both retain the high order accuracy and suppress numerical oscillations in the inner DOFs.

The rest of this article is organized as follows. Section 2 describes the framework of DGSEM on quadrilateral grids. The projection-WENO limiter described in Section 3 would introduce the L_2 projection in constructing the candidate polynomials and the WENO limiting procedure performed in the characteristic space. Numerical examples are given in Section 4 to validate the efficiency of the developed shock capturing scheme in computing compressible flows.

2   The DGSEM on unstructured quadrilateral grids

In this section we will review the implementation of DGSEM on unstructured quadrilateral grids in solving the inviscid compressible flows. The conservation form of the two-dimensional Euler equations can be written as

$$\frac{\partial U}{\partial t} + \frac{\partial F}{\partial x} + \frac{\partial G}{\partial y} = 0, \tag{1}$$

where U is the vector of the conservative variables given as $U = (\rho, \rho u, \rho v, \rho E)^T$, F, G are the inviscid flux vectors. The detailed formulations of the flux terms are well-known and are omitted here for brevity. The discontinuous Galerkin method uses the weak form of Eq. (1)

$$\int_{\Omega_i} \frac{\partial U}{\partial t} W d\Omega + \oint_{\partial \Omega_i} \vec{F}_n(U) \cdot \vec{n} W ds - \int_{\Omega_i} \vec{F}_n \cdot \nabla W d\Omega = 0, \vec{F}_n = (F, G), \tag{2}$$

where $\partial \Omega_i$ denotes the boundary of control volume Ω_i, $\vec{n}$ is the unit outward normal vector of the cell boundary, and W is the test function. In the second term, $\vec{F}_n(U) \cdot \vec{n}$ is the face inviscid flux denoted as $\hat{F}_n(U_i, U_{i+}, \vec{n})$ with $i+$ being the face-neighboring cell. The inviscid flux in this paper is evaluated by the Roe or HLL Riemann solver [18, 19].

The tensor-product of one-dimensional Gauss-Legendre (GL) points is taken as the solution points. An example for is shown in Fig. 1 for solution points of the $p2$ DGSEM. Using the solution points, the approximate solution is described as

$$U_i^h(\xi, \eta) = \sum_{m=1}^{p+1} \sum_{n=1}^{p+1} U_i^{mn} \psi_{mn}(\xi, \eta) = \sum_{m=1}^{p+1} \sum_{n=1}^{p+1} U_i^{mn} \varphi_m(\xi) \varphi_n(\eta), \tag{3}$$

where $\psi_{mn}(\xi, \eta) = \varphi_m(\xi)\varphi_n(\eta)$, with $\varphi_m(\xi), \varphi_n(\eta)$ being the one-dimensional Lagrangian interpolation basis following the definition

$$\varphi_m(\xi) = \prod_{k=1, k \neq m}^{p+1} \frac{\xi - \xi_k}{\xi_m - \xi_k}.$$

Thus the one-dimensional interpolation satisfies $\varphi_m(\xi_l) = \delta_{ml}$, with δ being the Kronecker symbol. $\xi_k, k = 1, ..., p+1$ are the abscissa values of the one-dimensional GL points. For brevity, we use the pk scheme to denote the scheme with approximate solution of k-th order polynomial.

Choosing the interpolation function $\psi_{kl}(\xi, \eta)$ as the test function W in Eq. (2), and substituting Eq. (3) into Eq. (2),
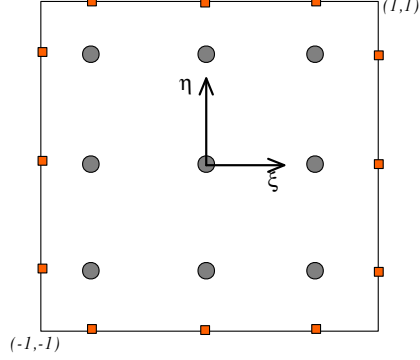
Figure 1: The distribution of solution points and face flux points on the quadrilateral grids for $p2$ DGSEM schemes. Solution point is marked in black dot and flux point in red square.

one can obtain

$$\sum_{m=1}^{p+1}\sum_{n=1}^{p+1}\frac{\partial U_i^{mn}}{\partial t}\int_{\Omega_i}\psi_{kl}\psi_{mn}d\Omega + \oint_{\partial\Omega_i}\hat{F}_n\left(U_i^h, U_{i+}^h, \vec{n}\right)\psi_{kl}ds - \int_{\Omega_i}\vec{F}_n\cdot\nabla\psi_{kl}d\Omega = 0. \tag{4}$$

For the mass matrix, the use of the tensor-product GL quadrature leads to

$$\int_{\Omega_i}\psi_{kl}\psi_{mn}d\Omega = \delta_{km}\delta_{ln}\omega_k\omega_l J_{k,l},$$

where $J_{k,l}$ is the Jacobian determinant in the (k,l)-th GL point of the control volume Ω_i, ω_k is the weight of GL quadrature. Thus the first term in Eq. (4) is simplified as $\frac{\partial U_i^{kl}}{\partial t}\omega_k\omega_l J_{k,l}$. The second term in Eq. (4) uses the GL quadrature on the face and the typical face flux points of $p2$ schemes are shown in Fig. 1 . The evaluation of variable values on the face flux points can use the one-dimensional interpolation, e.g., the value of the n-th flux point in the $\xi = 1$ face is

$$U_i^h\left(1, \eta_n\right) = \sum_{l=1}^{p+1}U_i^{ln}\varphi_l\left(1\right).$$

The gradient of interpolation function in the third term can be written as

$$\nabla\psi_{kl} = \mathbf{J}^{-1}\nabla_{\xi}\psi_{kl} = \left(\frac{\partial\varphi_k}{\partial\xi}\xi_x\varphi_l + \frac{\partial\varphi_l}{\partial\eta}\eta_x\varphi_k, \frac{\partial\varphi_k}{\partial\xi}\xi_y\varphi_l + \frac{\partial\varphi_l}{\partial\eta}\eta_y\varphi_k\right), \tag{5}$$

with the Jacobian matrix $\mathbf{J} = \frac{D(x,y)}{D(\xi,\eta)}$. Eq. (5) is used in evaluating ∇U_i^h and the third term of Eq. (4). Elements in the inverse Jacobian matrices $\xi_x, \xi_y, \eta_x, \eta_y$ are evaluated and stored for every solution points.

3   The projection-WENO limiter

One challenge for the high order limiter in DGSEM is to suppress the oscillations in the inner DOFs. A key ingredient of the projection-WENO limiter proposed in this section is the linear/bilinear candidate polynomials constructed through the L_2 projection in the central and face-neighboring cells. With a modified WENO weighted procedure, the final limited polynomial can smoothly switch from the high order one in the smooth region to the linear one near strong discontinuities.

3.1 The projection-WENO limiter on one-dimensional grids

3.1.1 The construction of the linear candidate polynomials

We first consider DGSEM on the one-dimensional grids. The numerical scheme is similar to the description in Section 2. The approximate solution in the central cell i (C_i) is written as,

$$U_i^h(\xi) = \sum_{l=1}^{p+1} U_i^l \varphi_l(\xi). \tag{6}$$

The linear candidate polynomials constructed for the limiting can be written as

$$U_{j \to i}(\xi) = \bar{U}_i + U_{\xi,j} \xi, \quad \xi = \frac{x - x_i}{2\Delta x}, \quad j \in \{i-1, i, i+1\}, \tag{7}$$

where x_i is the center of C_i and Δx is grid size of C_i. Thus this polynomial can conserve the mean value $\bar{U}_i$ on C_i. The gradient $U_{\xi,j}$ is obtained by minimizing the following value,

$$I_1 = \int_{C_j} (U_{j \to i}(x) - U_j(x))^2 \, dx.$$

The meaning of this formula is to find an approximate linear polynomial $U_{j \to i}(\xi)$ for $U_j(\xi)$ on C_j with minimum L_2 error. On the uniform one-dimensional grids, the gradient $U_{\xi,j}$ could be analytically expressed as

$$U_{\xi,i} = \frac{3}{2} \sum_{l=1}^{p+1} (U_i^l - \bar{U}_i) \omega_l \xi_l,$$

$$U_{\xi,i-1} = \frac{3}{26} \sum_{l=1}^{p+1} (U_{i-1}^l - \bar{U}_i) \omega_l (\xi_l + 2), \tag{8}$$

$$U_{\xi,i+1} = \frac{3}{26} \sum_{l=1}^{p+1} (U_{i+1}^l - \bar{U}_i) \omega_l (\xi_l - 2).$$

The linear candidate polynomials instead of high order candidate polynomials in [14, 15, 16] are constructed for the following reasons. First, a linear polynomial is much easier to construct especially on higher-dimensional grids. Second, high order limiter can also be constructed with linear candidates as described in the next section. Last and most important, a linear polynomial is better for oscillation suppressing in the inner DOFs of DGSEM. The source term in DGSEM needs a smooth polynomial across the whole cell. It is quite difficult to provide a high order smooth polynomial in a cell with strong shock waves.

3.1.2 The modified WENO limiter

From the last section, we have four candidate polynomials, the central high order one $U_i(\xi)$ and three constructed linear ones $U_{j \to i}(\xi), j \in \{i-1, i, i+1\}$ in Eq. (7). These candidate polynomials are transformed to the characteristic space and denoted as $V_0(\xi)$ for the central one and $V_1(\xi), V_2(\xi), V_3(\xi)$ for the three linear ones, with index $1, 2, 3$ denoting construction from cells $i-1, i, i+1$ respectively. The final weighted polynomial is

$$\tilde{v}(\xi) = w_0 v_0(\xi) + w_1 v_1(\xi) + w_2 v_2(\xi) + w_3 v_3(\xi), \tag{9}$$

where v is one component of V. The weights w_l are defined as

$$w_l = \frac{\alpha_l}{\sum_{k=0}^3 \alpha_k}, \alpha_l = \frac{\lambda_l}{\beta_l^2 + \varepsilon_l}, l = 0, 1, 2, 3. \tag{10}$$

The WENO smooth indicator is evaluated as

$$\beta_0 = \sum_{k=1}^{p} \int_{-1}^{1} \left(\frac{\partial v_0^k(\xi)}{\partial^k \xi} \right)^2 d\xi,$$

$$\beta_l = 2v_{\xi,l}^2, l = 1, 2, 3. \tag{11}$$

where β_0 is equivalent to the below one in the physical coordinate,

$$\beta_0 = \sum_{k=1}^{p} \int_{C_i} \left(\frac{\Delta x}{2} \right)^{2k-1} \left(\frac{\partial v_0^k(x)}{\partial^k x} \right)^2 dx. \tag{12}$$

This smooth indicator is a slight modification of the classical one in [20] on the length scale and can work better in the proposed limiter here. The analytical expression for calculating β_0 is referred to Appendix A. In Eq. (10), the linear weights λ are chosen as

$$\lambda_1 = \lambda_3 = 1, \lambda_2 = 100, \lambda_0 = 10^{2p} = \begin{cases} 10^2, & p = 1; \\ 10^4, & p = 2; \\ 10^6, & p = 3, \end{cases}$$

to emphasize the contribution of polynomials in the central cell. ε_0 is chosen to be 10^{-16} preventing the denominator from being 0. Since $\beta_l(l = 1, 2, 3)$ could be very close to 0 near the extrema, we need to set a relatively large value for the WENO small $\varepsilon_l(l = 1, 2, 3)$ for better accuracy. Whereas large values of ε_l might cause numerical oscillations. A careful choice for ε_l will be discussed later.

After the limiting of each characteristic variable, the limited polynomials $\tilde{V}(\xi)$ in the characteristic space are transformed back to $\tilde{U}_i(\xi)$ in the conservative space. Finally $\tilde{U}_i(\xi)$ is used to evaluate the DOFs on C_i,

$$\tilde{U}_i^l = \tilde{U}_i^l(\xi_l), \tag{13}$$

where ξ_l is the local coordinate of the l-th solution point.

The Shu-Osher [21] and Lax tube [22] problems are used to study the effect of WENO small ε_l on the accuracy and shock capturing abilities. No shock detector is used in the calculation. To simplify the discussion, we first set $\varepsilon_2 = \varepsilon_1 + \varepsilon_3$. The results using constant $\varepsilon_1 = \varepsilon_3 = 10^{-6}$ and 10^{-4} are shown in Figs. 2 and 3. The shock-vortex interaction in the Shu-Osher problem is well captured in higher resolution with larger ε and no numerical oscillations are generated. In Lax tube problem, smaller ε can suppress numerical oscillations with much lower magnitude. Thus large ε could only capture weak shock waves and preserve higher order accuracy, while small ε could capture the strong shock waves with more numerical diffusion. To preserve the numerical accuracy and capture strong shocks simultaneously, ε is varied according to the discontinuity strength (DS) and the following function is designed,

$$\varepsilon_k = 10^{-12/\pi \cdot \arctan(\mathrm{DS} - \mathrm{DS}_{\mathrm{strong}}) - 6}, k = 1, 3, \text{ with } \mathrm{DS} = \frac{\left| \rho_k^L - \rho_k^R \right|}{\Delta x^{(p+1)/2} \bar{\rho}_i}, \mathrm{DS}_{\mathrm{strong}} = \begin{cases} 1, & p = 1; \\ 5, & p = 2; \\ 50, & p = 3, \end{cases} \tag{14}$$

$$\varepsilon_2 = \varepsilon_1 + \varepsilon_3,$$

where $\rho_k^{L/R}$ are the left and right density values at the cell interface. DS takes a very similar form as the KXRCF shock detector [23], but is evaluated on the face instead of the cell. The ε in Eq. (14) can change from 1 to 10^{-12} smoothly near $\mathrm{DS} = \mathrm{DS}_{\mathrm{strong}}$ as indicated in Fig. 4. The results using the varied ε are shown in Fig. 5. We could observe that the projection-WENO limiter with varied ε can suppress the numerical oscillation near strong shocks and capture the shock-vortex interaction in high resolution. Two more test cases, the Sod tube problem [22] and the interaction of two blast waves [24], are calculated and the results shown in Fig. 6 contain very few numerical oscillations.

The projection-WENO limiter with the parameters ε, λ chosen in the above section can be accuracy preserving in smooth regions. According to Eq. (14), ε is larger than 10^{-6} on weak shock regions and of order $O(1)$ to $O(10^{-2})$ on smooth regions. The smoothness indicators β_0 and $\beta_l, l = 1, 2, 3$ are of $O(\Delta x^2)$ according to [20] and are denoted as,

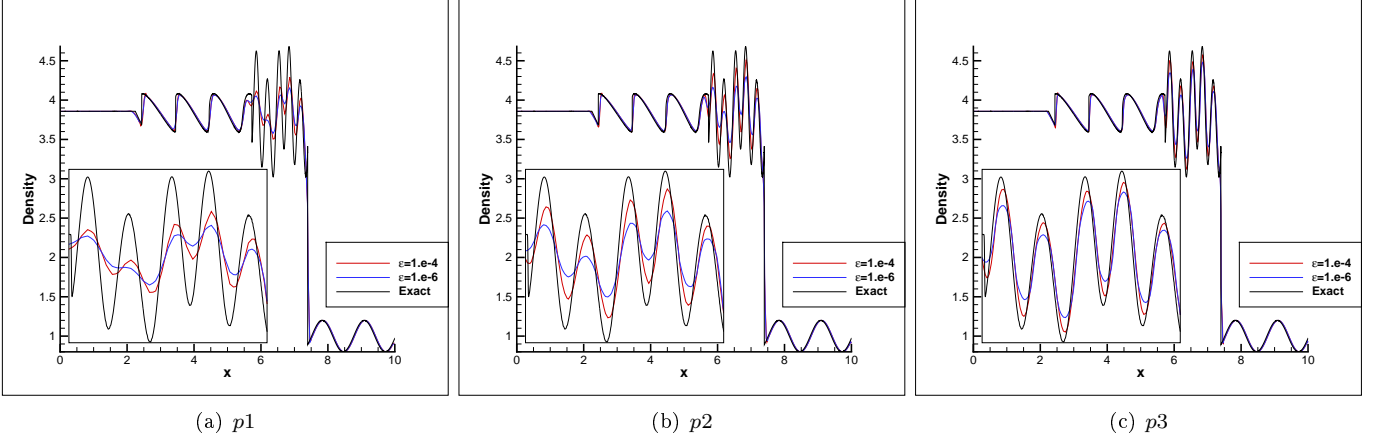$$\beta_0 = C_0 \Delta x^2, \beta_l = C_l \Delta x^2, l = 1, 2, 3.$$

Figure 2: Shu-Osher problem with $\varepsilon = 10^{-4}$ and 10^{-6}. Grid number is 200 and all DOFs are plotted.

C_0 and C_l are of the same magnitude away from extrema and C_l approximates 0 near extrema. The WENO weight w_0 is then evaluated as (ε_0 is very small and omitted here),

$$w_0 = \frac{\frac{10^{2p}}{C_0^2 \Delta x^4}}{\frac{10^{2p}}{C_0^2 \Delta x^4} + \frac{100}{C_2^2 \Delta x^4 + \varepsilon_2} + \sum_{l=1,3} \frac{1}{C_l^2 \Delta x^4 + \varepsilon_l}}. \tag{15}$$

When cell i is away from extrema, Eq. (15) leads to

$$w_0 > \frac{10^{2p}}{10^{2p} + 100(C_0/C_2)^2 + (C_0/C_1)^2 + (C_0/C_3)^2}. \tag{16}$$

When cell i is near extrema, Eq. (15) leads to

$$w_0 > \frac{10^{2p}}{10^{2p} + \Delta x^4 C_0^2 (100/\varepsilon_2 + 1/\varepsilon_1 + 1/\varepsilon_3)}. \tag{17}$$

In the denominator of Eq. (16), C_0 and C_l are of the same magnitude; in Eq. (17), $\varepsilon_l, l = 1, 2, 3$ is of order $O(1)$ to $O(10^{-2})$ on smooth regions. Thus 10^{2p} is much larger than other three terms whether near or away from extrema. We can conclude that w_0 is very close to 1. Although it is difficult to rigorously prove the order of accuracy after applying the limiter, numerical experiments of this paper verify that the present limiter is accuracy preserving for smooth flows.

[Remark 1] The projection-WENO limiter is different from the traditional WENO limiter in finite difference or discontinuous Galerkin methods [25, 15, 16]. First and foremost, the construction way and the degree for the candidate polynomials are different. Second, the WENO smooth indicator is slightly modified. The current smoothness indicator β_0 places less emphasis on high order derivatives as shown in Eq. (12). Third, the WENO small ε is related with the discontinuity strength DS.

[Remark 2] Unlike the shock detector, the discontinuity strength DS is used to adjust the diffusion in the limiter. The threshold DS_{strong} is used to estimate the strong shock waves. As indicated in Fig. 4, when $DS < DS_{strong}$, ε will smoothly increase to 1 which is small enough to capture the weak shocks. When $DS > DS_{strong}$, ε decreases to 10^{-12} and the final limited polynomial will be approximately a linear one. Although there exist some other ways to improve the accuracy by modifying ε such as [26], Eq. (14) is a new one and more suitable to use in DGSEM. Parameters ε, DS and DS_{strong} are used to adjust the dissipation in the limiter and their forms are still under improvement.

3.2 Extension to unstructured quadrilateral grids

This section generalizes the projection-WENO limiter in Section 3.1 to unstructured quadrilateral grids. It is not a straightforward job. The candidate linear polynomials cannot be easily obtained through the face-neighboring cells since
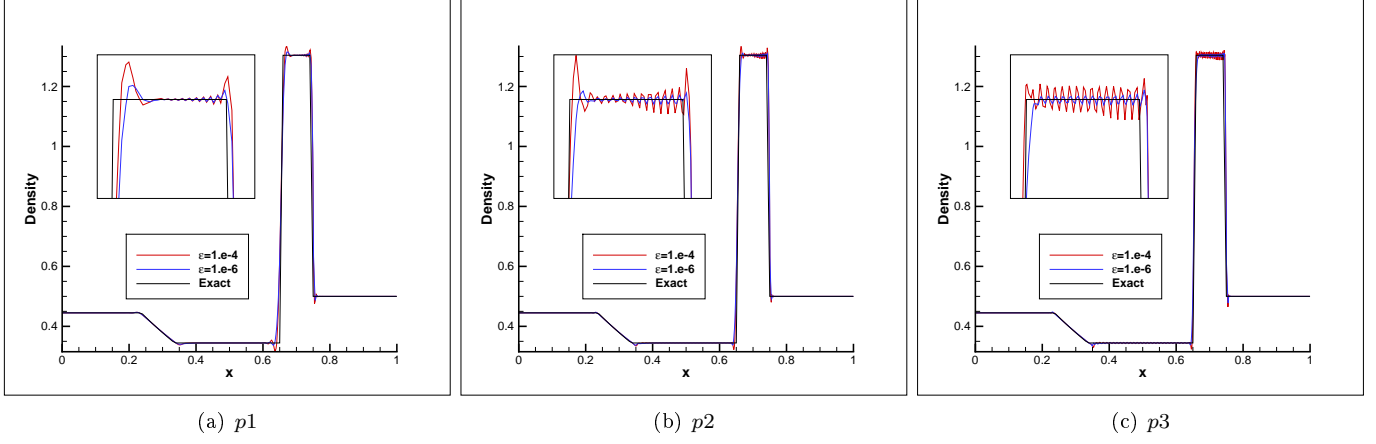
6

(a) $p1$ (b) $p2$ (c) $p3$

Figure 3: Lax tube problem with $\varepsilon = 10^{-4}$ and 10^{-6}. Grid number is 200 and all DOFs are plotted.

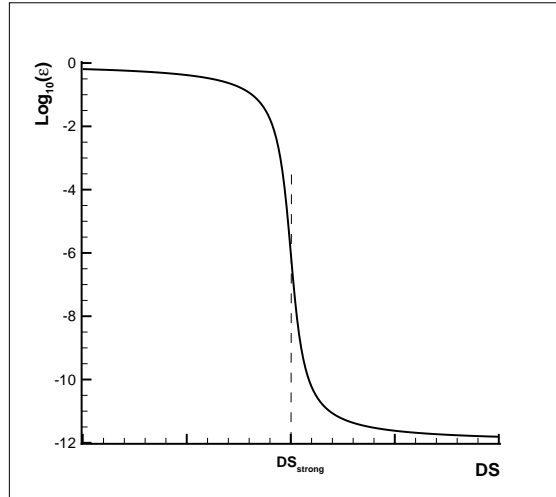Figure 4: The relation curve between ε and DS.
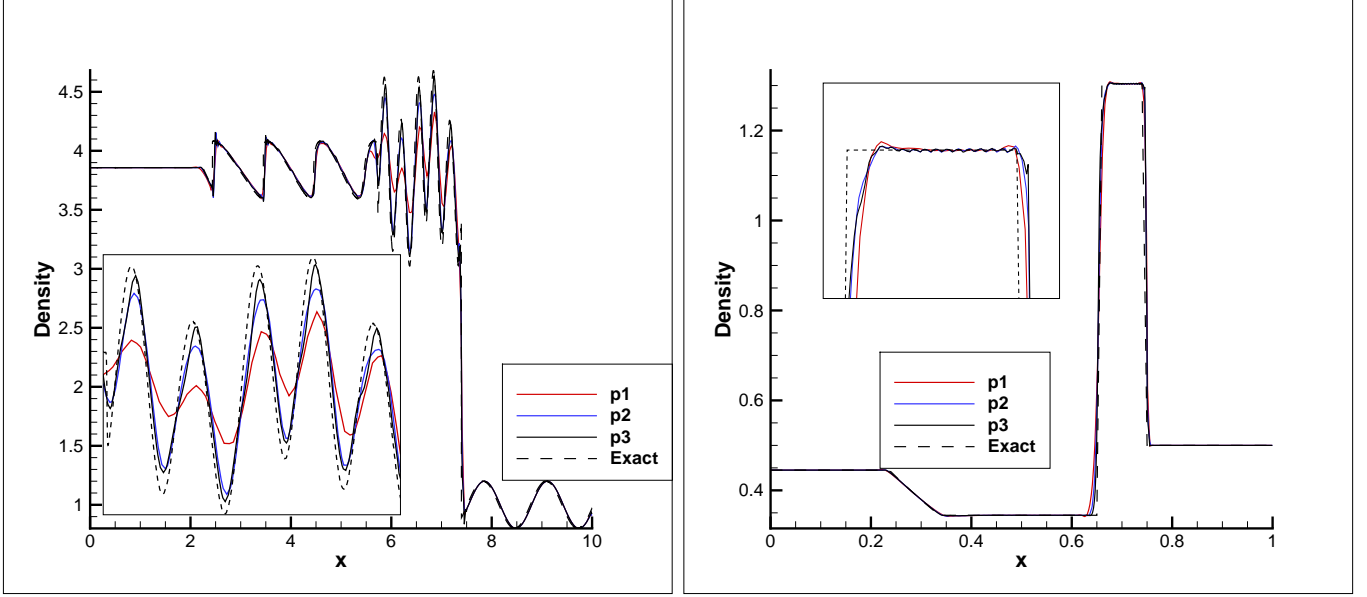
Figure 5: The Shu-Osher (left) and Lax tube (right) problems with varied ε in Eq. (14). Grid number is 200 and all DOFs are plotted.
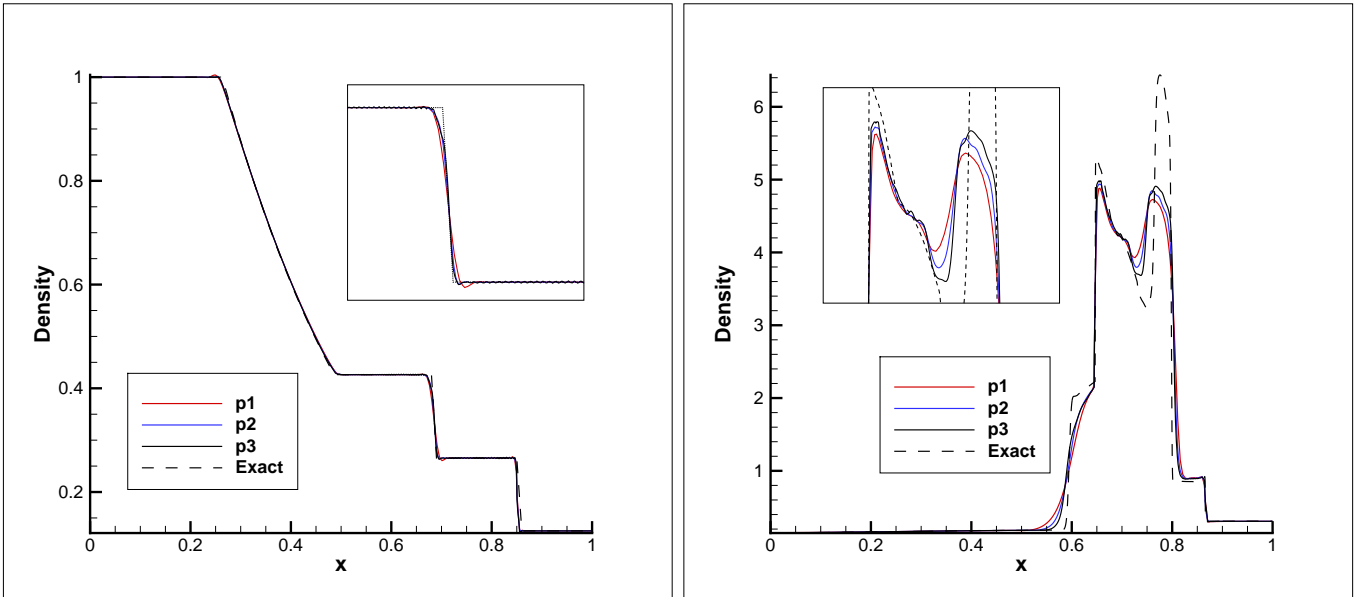

Figure 6: The Sod tube (left) and two blast waves interaction (right) problems with varied ε in Eq. (14). Grid number is 200 and all DOFs are plotted.
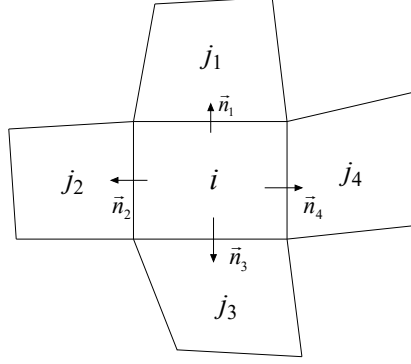
Figure 7: The limiting stencils $T_i = \{j_1, j_2, j_3, j_4\}$ in unstructured quadrilateral grids.

the local iso-prametric coordinates are used in each cell as described in Section 2. The WENO weight will be very time consuming on the multi-dimensional grids. This section will give a simple way to construct the linear candidate polynomials and perform the limiting through the dimension-by-dimension way to reduce computational cost.

Firstly a bilinear polynomial is constructed in physical coordinates using the mean value in the central cell,

$$u1(x,y) = \bar{u}_i + u_x X + u_y Y + u_{xy}(XY - \overline{XY}), X = x - x_i, Y = y - y_i, \overline{XY} = \frac{1}{V_i}\int_{\Omega_i} XY d\Omega, \tag{18}$$

where u is a component of conservative variables U, (x_i, y_i) is the gravity center and V_i is the area of cell i. The coefficients u_x, u_y and u_{xy} are obtained by minimizing the value

$$I_2 = \int_{\Omega_j} (u1(x,y) - u_j(\xi,\eta))^2 d\Omega, \ j \in T_i = \{j_1, j_2, j_3, j_4\}.$$

The stencil T_i is shown in Fig. 7. By solving the equations

$$\frac{\partial I_2}{\partial u1_x} = 0, \frac{\partial I_2}{\partial u1_y} = 0, \frac{\partial I_2}{\partial u1_{xy}} = 0,$$

the coefficients in Eq. (18) can be obtained.

Then we interpolate the values in solution points in cell i and have the candidate polynomial, $u_{j\to i}(\xi,\eta)$, following the same form of $u_i(\xi,\eta)$ in Eq. (3),

$$u_{j\to i}(\xi,\eta) = \sum_{m=1}^{p+1}\sum_{n=1}^{p+1} u_{j\to i}^{mn}\varphi_m(\xi)\varphi_n(\eta), \ \text{with} \ u_{j\to i}^{mn} = u1(x_i^{mn}, y_i^{mn}), j \in T_i.$$

where (x_i^{mn}, y_i^{mn}) is the physical coordinate of the mn-th solution point in cell i. Using the central and four candidate polynomials, the limiting procedure combines the projection-WENO limiter in Section 3.1 and the time-saving characteristic limiting idea in [27]. Detailed steps are described as follows.

(1). For the f-th face with the direction $\vec{n}_f$, transform the polynomial $U_i(\xi,\eta)$ and $U_{j_f\to i}(\xi,\eta)$ to the characteristic space which are denoted as $V_0(\xi,\eta)$ and $V_f(\xi,\eta)$ respectively. One component of the characteristic polynomials is expressed as

$$v_k(\xi,\eta) = \sum_{m=1}^{p+1}\sum_{n=1}^{p+1} v_k^{mn}\varphi_m(\xi)\varphi_n(\eta), k = 0, f.$$

(2). For the g-th face flux point on the f-th face, we extract the 1D line values which are used to interpolate this flux point and form the 1D polynomial. Specifically speaking, if the f-th face is in the ξ direction, the 1D polynomials are

$q_0(\xi), q_1(\xi)$, defined as

$$q_0(\xi) = \sum_{l=1}^{p+1} q_0^l \varphi_l(\xi), \; q_0^l = v_0^{lg},$$

$$q_1(\xi) = \sum_{l=1}^{p+1} q_1^l \varphi_l(\xi), \; q_1^l = v_f^{lg}.$$

The candidate polynomials are the high order polynomial $q_0(\xi)$ and the linear ones $s_0(\xi)$ and $s_1(\xi)$, which are obtained by projecting $q_0(\xi)$ and $q_1(\xi)$ to linear polynomials using the first formula in Eq. (8).
(3). Perform the WENO limiting procedure following Section 3.1.2 for all the face flux points on the f-th face. The final limited polynomial $\tilde{V}_f(\xi, \eta)$ is obtained in the characteristic space on the f-th face. Transform back to the conservative space and we have $\tilde{U}_f(\xi, \eta)$.
(4). Perform the above limiting steps (1) to (3) for all the four faces of cell i and four limited polynomial, $\tilde{U}_f(\xi, \eta), f = 1, \cdots, 4$, can be obtained. The final limited polynomial would be the arithmetic average of the four polynomials,

$$\tilde{U}(\xi, \eta) = \frac{1}{4} \sum_{f=1}^{4} \tilde{U}_f(\xi, \eta). \tag{19}$$

The comment for the limiting procedure is given in the following remarks.

[Remark 1] The limiting on quadrilateral grids fully utilizes the tensor-product property of the approximate solution. The limiter could be applied on high order quadrilateral grids without special treatment and is computationally efficient comparing with other multi-dimensional WENO limiters such as [16].
[Remark 2] In step (3), the number of candidate polynomials is one less than that in Section 3.1.2. We do not consider, e.g., j_1 and j_3, as a pair like the 1D case for $\vec{n}_1$ and $\vec{n}_3$ are not parallel on general quadrilateral grids.
[Remark 3] The characteristic limiting way adopted from [16] could provide better numerical accuracy and be robust in shock capturing. An ongoing job engages on the nonlinear wighting in the final conservative space instead of the simple arithmetic average in Eq. (19).

4   Numerical tests

The cases in Sections 4.1, 4.2 and 4.3 are calculated without any shock detectors to demonstrate the high order accuracy of the developed limiter. Eq. (14) is used to evaluate ε by default, and also constant ε is used in the accuracy study for comparisons. The time consuming cases in Sections 4.4 are calculated with a modified KXRCF detector adopted by [17],

$$S_i = \frac{\left| \int_{\partial \Omega_i^-} \left(u_i^h - u_j^h \right) ds \right|}{h \left| \partial \Omega_i^- \right| \bar{u}_i M_p}, \tag{20}$$

where h is the grid size, $\partial \Omega_i^-$ denotes the surface of cell i through which the fluid flows into cell i, and cell j is adjacent to cell i with $\partial \Omega_i^-$ as the interface. $\bar{u}_i$ is the cell average on cell i and u is chosen to be the density in this paper. M_p is chosen to be 0.2 for all cases. When $S_i > 1$, cell i is marked as the troubled cell.

All the contours are output with $(p+1)^2$ uniform quadrilateral sub-cells shown in Fig. 8 to display all the inner DOFs of the DGSEM.

4.1   Accuracy study on the projection-WENO limiter

4.1.1   Isentropic vortex problem

The isentropic vortex transport problem [28] is used to examine the accuracy of numerical schemes in computing multi-dimensional flows without shock waves. The mean flow is $\rho = 1, p = 1$, and $(u, v) = (1, 1)$. We add, to mean flow, an
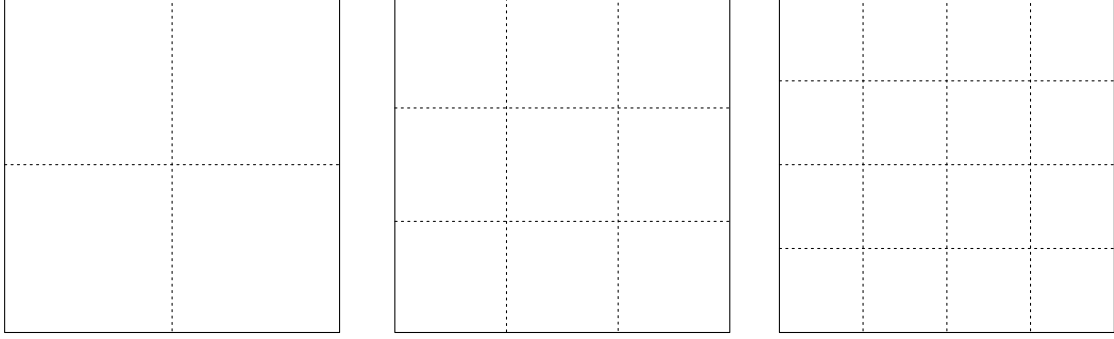
Figure 8: The sub-cells for outputting the inner DOFs of $p1$ to $p3$ DGSEM schemes from left to right respectively.

Table 1: Accuracy study on the project-WENO limiter using the isentropic vortex problem.

Scheme	Grid	Unlimited		Projection-WENO, $\varepsilon = 10^{-6}$		Projection-WENO, ε uses Eq. (14)	
		L_2 error	Order	L_2 error	Order	L_2 error	Order
$p1$	h=1	1.054E-02		2.607E-02		1.246E-02	
	h=1/2	2.330E-03	2.18	4.607E-03	2.50	2.379E-03	2.39
	h=1/4	5.044E-04	2.21	5.885E-04	2.97	5.049E-04	2.24
	h=1/8	1.183E-04	2.09	4.389E-06	7.07	1.183E-04	2.09
$p2$	h=1	1.517E-03		1.914E-02		1.522E-03	
	h=1/2	1.873E-04	3.02	1.662E-03	3.53	1.871E-04	3.02
	h=1/4	2.010E-05	3.22	8.691E-05	4.26	2.010E-05	3.22
	h=1/8	2.314E-06	3.12	4.389E-06	4.31	2.314E-06	3.12
$p3$	h=1	2.552E-04		1.423E-02		2.553E-04	
	h=1/2	1.544E-05	4.05	2.991E-04	5.57	1.544E-05	4.05
	h=1/4	7.978E-07	4.27	2.771E-06	6.75	7.978E-07	4.27
	h=1/8	4.469E-08	4.16	1.028E-07	4.75	4.469E-08	4.16

isentropic vortex expressed by the following perturbations,

$$(\delta u, \delta v) = \frac{\chi}{2\pi} e^{0.5(1-r^2)} \left(-\bar{y}, \bar{x} \right),$$

$$\delta T = -\frac{(\gamma - 1)\varepsilon^2}{8\gamma\pi^2} e^{1-r^2}, \quad \delta S = 0,$$

with $(\bar{x}, \bar{y}) = (x - 5, y - 5), r^2 = \bar{x}^2 + \bar{y}^2$, and the vortex strength $\chi = 5$. The computational domain is taken as $[0, 10] \times [0, 10]$, and periodic boundary conditions are used. We compute the solution at $t = 2.0$ to test the accuracy of DGSEM schemes on uniform quadrilateral grids of size $h = 1, 1/2, 1/4$ and $1/8$.

The L_2 errors with $p1$ to $p3$ unlimited and limited DGSEM schemes are shown in Table 1. We can observe that all the schemes can achieve the expected orders. The limited DGSEM schemes with ε in Eq. (14) give almost the same errors as the unlimited schemes, while the limited DGSEM schemes with constant $\varepsilon = 10^{-6}$ are more dissipative and give larger errors.

4.1.2 Accuracy study on subsonic flows around the cylinder

The subsection uses the subsonic flow past a circular cylinder at a Mach number of inlet Mach number $Ma_\infty = 0.38$. The purpose is to validate the accuracy of DGSEM schemes on quadrilateral grids with curved wall boundary. The four successively refined o-type grids having 16×5, 32×9, 64×17, and 128×33 grid points are used for the calculation and the former three ones are shown in Fig. 9. Details on generating such grids can be referred to [8]. The following entropy

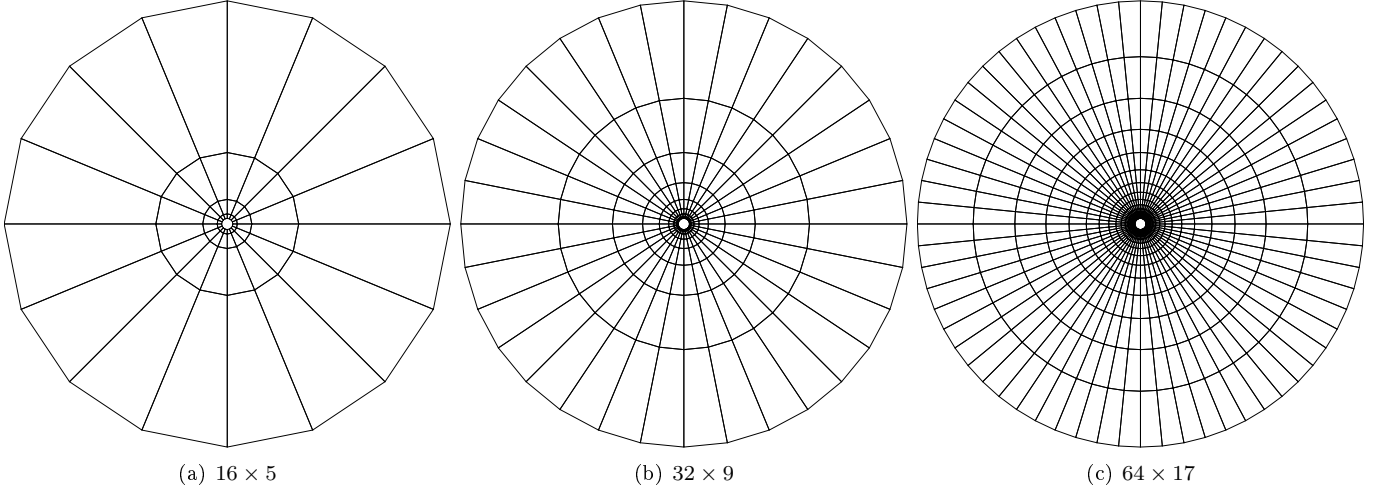| (a) 16×5 | (b) 32×9 | (c) 64×17 |

Figure 9: The series of refined quadrilateral grids for calculating the subsonic flow around the cylinder.

Table 2: Accuracy study on the project-WENO limiter using the subsonic flow around the cylinder

Scheme	Grid	Unlimited		Projection-WENO, $\varepsilon = 10^{-6}$		Projection-WENO, ε uses Eq. (14)	
		L_2 error	Order	L_2 error	Order	L_2 error	Order
$p1$	16×5	2.662E-03		3.451E-03		2.813E-03	
	32×9	5.311E-04	2.33	6.302E-04	2.45	5.419E-04	2.38
	64×17	8.965E-05	2.57	9.474E-05	2.73	8.985E-05	2.59
	128×33	1.453E-05	2.63	1.481E-05	2.68	1.453E-05	2.63
$p2$	16×5	5.534E-04		1.207E-03		5.013E-04	
	32×9	4.865E-05	3.51	6.969E-05	4.11	4.863E-05	3.37
	64×17	5.073E-06	3.26	4.179E-06	4.06	5.080E-06	3.26
	128×33	6.321E-07	3.00	6.320E-07	2.73	6.318E-07	3.01
$p3$	16×5	4.312E-05		1.934E-04		4.319E-05	
	32×9	1.414E-06	4.93	3.054E-06	5.98	1.415E-06	4.93
	64×17	6.117E-08	4.53	1.462E-07	4.38	6.116E-08	4.53

production ε defined as

$$\varepsilon = \frac{S - S_\infty}{S_\infty} = \frac{p}{p_\infty} \left(\frac{\rho_\infty}{\rho} \right)^\gamma - 1,$$

is served as the error measurement, where S is the entropy. In this case, HLL Riemann solver is used.

The L_2 errors on a series of refined quadrilateral grids with $p1$ to $p3$ unlimited and limited DGSEM schemes are shown in Table 2. Similar to the analysis in Section 4.1.1, all the schemes can achieve the expected orders. The limited DGSEM schemes with ε in Eq. (14) give almost the same errors as the unlimited schemes, while the limited DGSEM schemes with constant $\varepsilon = 10^{-6}$ is more dissipative and give larger errors. The limited schemes exhibit good accuracy and convergence properties in the steady flows.

4.2 Two-dimensional Riemann problems

This subsection tests the performance of the project-WENO limiter in computing multi-dimensional waves over a broader range of conditions. We consider a two-dimensional region $[-1, 1] \times [-1, 1]$ that is partitioned into four zones, $[-1, -1] \times [0, 0]$ for zone 1, $[0, -1] \times [1, 0]$ for zone 2, $[0, 0] \times [1, 1]$ for zone 3, $[-1, 0] \times [0, 1]$ for zone 4. The grids are composed of 80×80 uniform quadrilaterals. Two different initial settings are selected from [29] and listed in Table 3. HLL Riemann solver is used. The calculation has been performed to $t = 0.52$.

The results are shown in Fig. 10. Few numerical oscillations generate near the discontinuities for $p1$ to $p3$ schemes.

Table 3: Initial conditions of two-dimensional Riemann problems.

	Problem I				Problem II			
	zone 1	zone 2	zone 3	zone 4	zone 1	zone 2	zone 3	zone 4
ρ	0.8	1	0.5197	1	0.8	1	0.5313	1
u	0.1	0.1	0.1	-0.6259	0	0	0	0.7276
v	0.1	-0.6259	0.1	0.1	0	0.7276	0	0
p	1	1	0.4	1	1	1	0.4	1

Higher order schemes show sharper gradients near discontinuities and capture more small flow structures than lower order ones.

4.3   The diffraction of a supersonic shock moving over a 90° corner

This case is taken from [30]. The shock Mach number is 5.09. The computational domain is a unit square $[0,1]\times[0,1]$. The corner is at $(x,y) = (0.05, 0.625)$ and the region $[0,0.05]\times[0,0.625]$ is solid. Initially, the shock is at $x = 0.05$. To the right of the shock, the flow field is initialized to

$$(\rho, u, v, p)_R = (1.4, 0, 0, 1).$$

To the left of the shock, the flow variables are computed using moving shock relations, i.e.,

$$(\rho, u, v, p)_L = (7.04113, 4.07795, 0, 30.0595).$$

At the left, right, and bottom boundaries, all flow quantities are prescribed. At the top, time-dependent conditions determined by the exact motion of the shock are used, i.e.

$$(\rho, u, v, p) = \begin{cases} (\rho, u, v, p)_L, & \text{if } x < 5.09t; \\ (\rho, u, v, p)_R, & \text{if } x > 5.09t. \end{cases}$$

The solid walls are treated using the reflecting boundary condition. Two kinds of uniform quadrilateral grids, $h = 1/80$ and $h = 1/160$, are used in the calculation. HLL Riemann solver is used.

The $p1$ to $p3$ schemes are used in the calculation and the results are shown in Fig. 11. Few numerical oscillations generate near the discontinuities for three numerical schemes. Higher order schemes show sharper gradients near discontinuities and capture more small flow structures than lower order ones.

4.4   Double Mach reflection problem

One of the popular test cases for high-resolution schemes is the double Mach reflection problem [24]. The whole computational domain is $[0,4] \times [0,1]$ with uniform quadrilateral grids of size $h = 1/120$. The wall is located at the bottom of the computational domain beginning at $x = 1/6$. Initially, a right-moving shock with $Ma = 10$ is located at $x = 1/6, y = 0$, inclined 60° with respect to the x-axis. HLL Riemann solver is used. The computation is carried out until $t = 0.2$.

The $p1$ to $p3$ DGSEM schemes are used for the calculation. The shock region marked by the modified KXRCF detector in Eq. (20) is shown in Fig. 12. The density contours shown in Fig. 13 indicate that the numerical oscillations are small for different orders of schemes. From Fig. 14 we can observe that higher order schemes capture more detailed flow structures near the Mach stem than lower order schemes.

5   Conclusions

This paper proposed a high-order projection-WENO limiter for the shock capturing for DGSEM schemes on quadrilateral grids. Unlike the traditional WENO limiters, the projection-WENO limiter weights the high order polynomial in the central cell and linear ones from the central and face-neighboring cells. A L_2 projection is used to construct all linear candidate polynomials. The limiting procedure uses the modified WENO weight, which changes the smooth indicator and
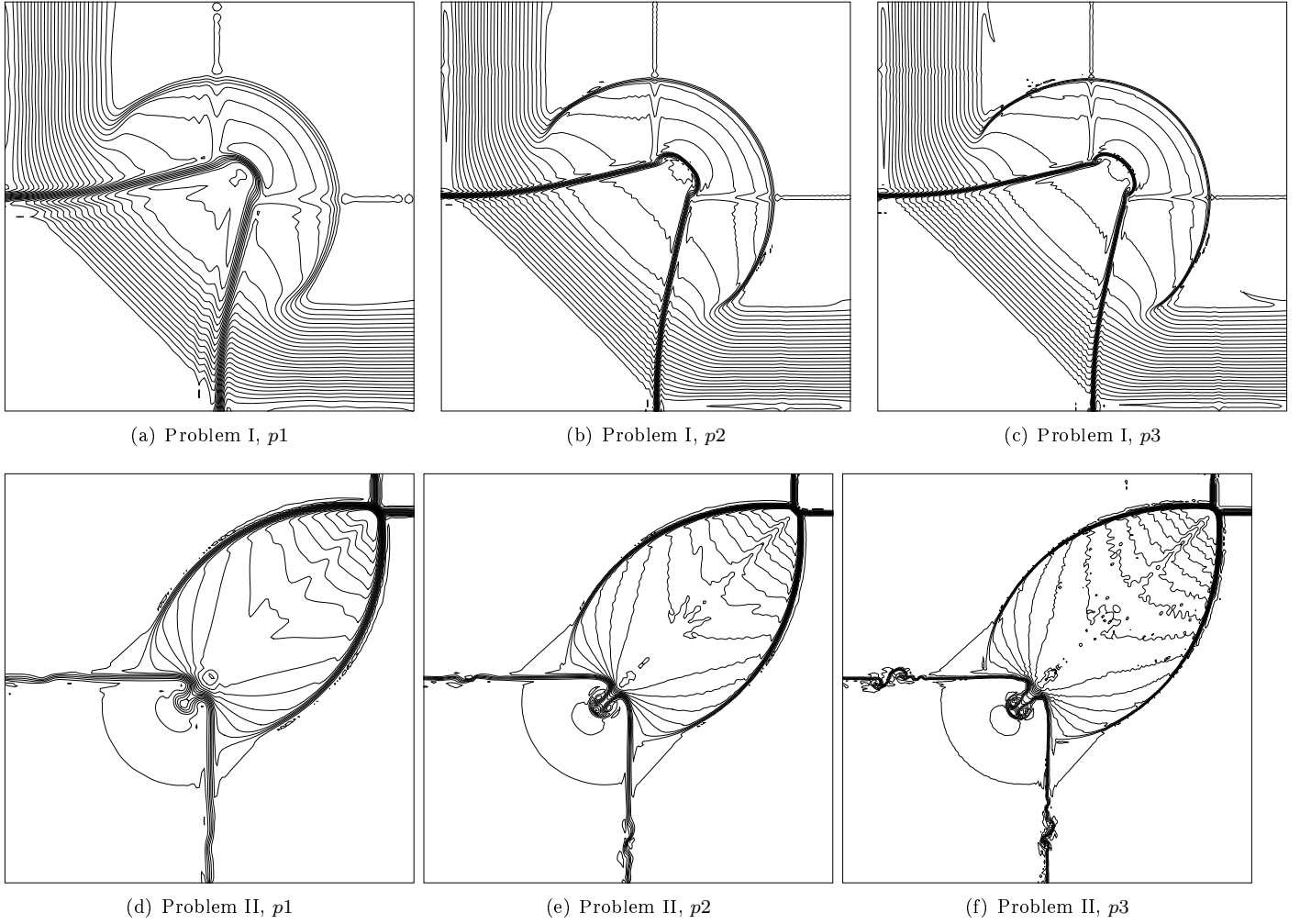
(a) Problem I, $p1$ (b) Problem I, $p2$ (c) Problem I, $p3$

(d) Problem II, $p1$ (e) Problem II, $p2$ (f) Problem II, $p3$

Figure 10: Density contour for the two 2D Riemann problems using $p1$ to $p3$ DGSEM schemes. Quadrilateral grid size is $h = 1/40$ on the region [-1,1]×[-1,1].
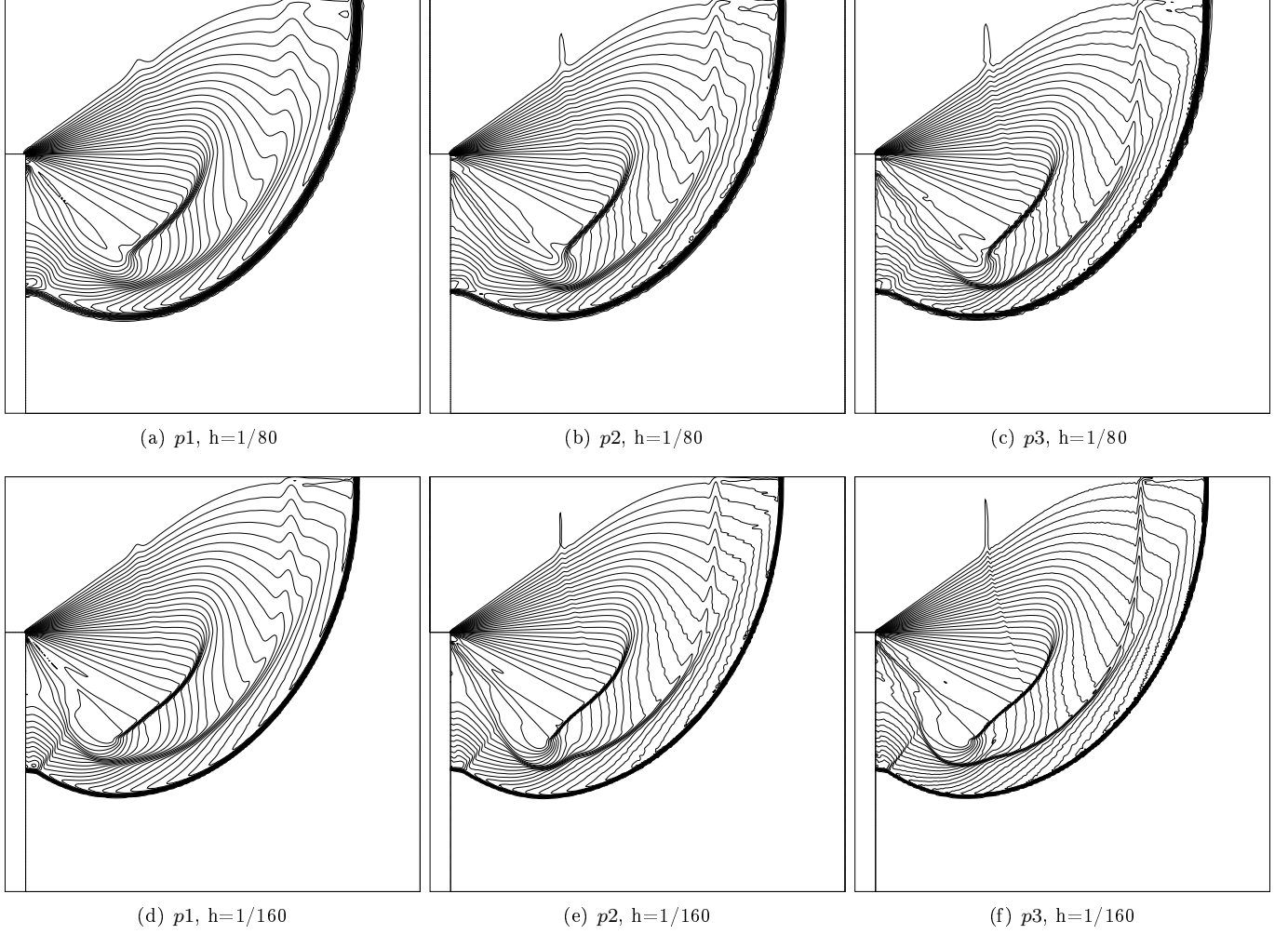
(a) $p1$, h=1/80   (b) $p2$, h=1/80   (c) $p3$, h=1/80

(d) $p1$, h=1/160   (e) $p2$, h=1/160   (f) $p3$, h=1/160

Figure 11: Density contours for the diffraction of a supersonic shock moving over a 90° corner using $p1$ to $p3$ (from left to right) DGSEM schemes. Quadrilateral grids size is $h = 1/80$ on the up side and $h = 1/160$ on the down side on the region [0,1]$\times$[0,1].
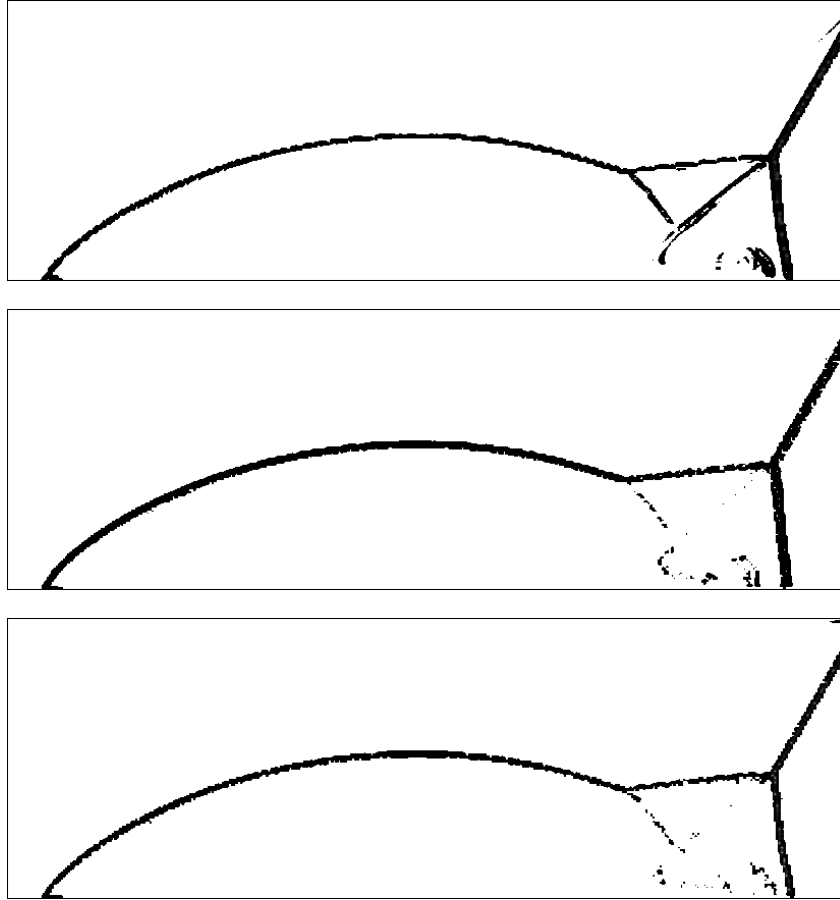
Figure 12: The shock region marked by the modified KXRCF detector for double Mach reflection with grid size $h = 1/120$ using $p1$ to $p3$ (from top to bottom) DGSEM schemes.
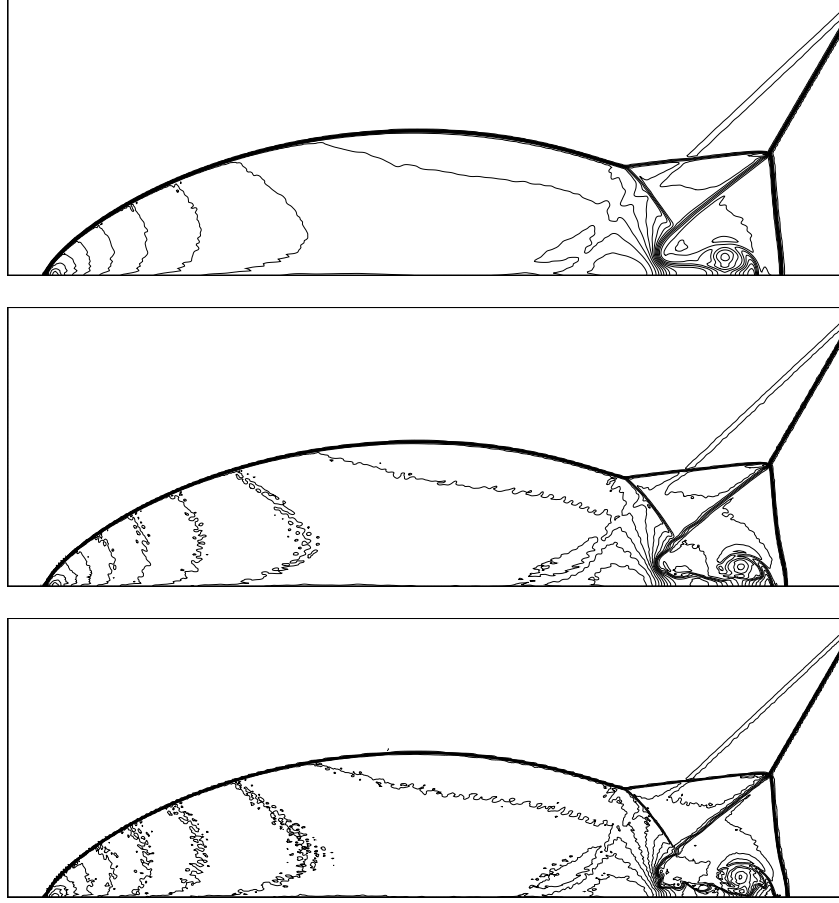
Figure 13: Density contours for double Mach reflection with grid size $h = 1/120$ using $p1$ to $p3$ (from top to bottom) DGSEM schemes . Thirty equally spaced contour lines from $\rho = 1.7$ to 21.5.
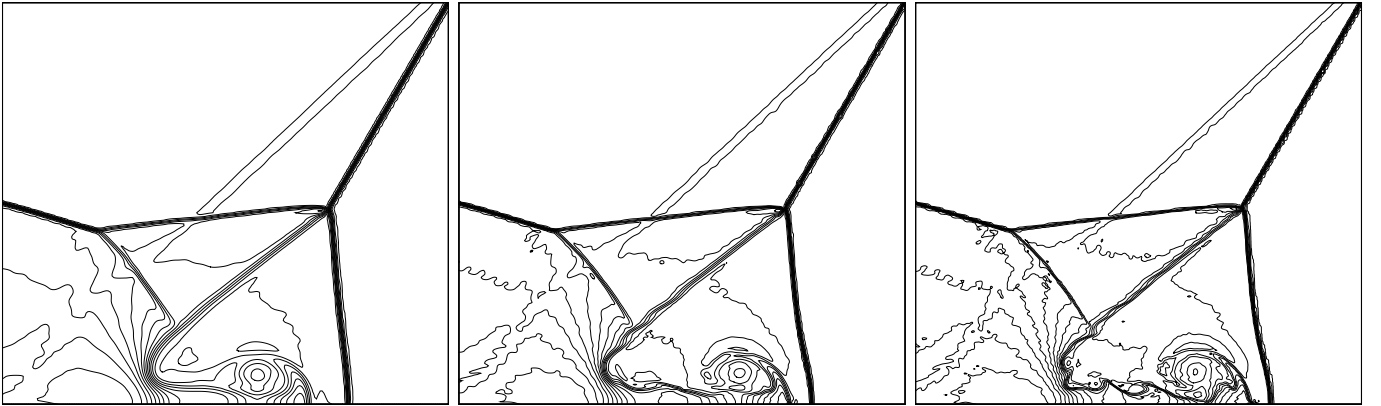

Figure 14: Machstem density contours for double Mach reflection with grids of size $h = 1/120$ using $p1$ to $p3$ (from left to right) DGSEM schemes. Thirty equally spaced contour lines from $\rho = 1.7$ to 21.5.

relates the WENO small ε with the discontinuity strength for better shock-capturing and accuracy-preserving capabilities. The extension to quadrilateral grids uses the construction of bilinear candidate polynomials and performs the limiting in a dimension-by-dimension way. The shock capturing ability is verified through abundance of test cases including the accuracy study, inviscid and viscous shock flows. This work will continue to validate the projection-WENO limiter for DGSEM on hexahedral grids in calculating three-dimensional turbulent flows with shock waves.

Acknowledgments

Appendix

A   The expression of the smoothness indicator

For evaluating the smoothness indicator in Eq. (11), we use one component a_k to denote the DOF v_0^k in the polynomial $v_0(\xi)$. The smoothness indicator β_0 for $p1$ polynomial is

$$\beta_0 = \frac{3}{2}(a_1 - a_2)^2.$$

β_0 for $p2$ polynomial is

$$\beta_0 = ((16 + 3s^2)a_1^2 + 64a_2^2 - 64a_2 a_3 + (16 + 3s^2)a_3^2 + a_1(-64a_2 + 32a_3 - 6s^2 a_3))/(6s^4), s = \sqrt{6}.$$

β_0 for $p3$ polynomial is

$$
\begin{aligned}
\beta_0 =& (3s^2(249 + 5s^2(-2 + s^2))(a_2 - a_3)^2 - 30q^3 s(-1 + s^2)(a_2 - a_3)(a_1 - a_4) + 6qs(-249 + 5s^2)(a_2 - a_3)(a_1 - a_4) - \\
& 30q^4(a_1 - a_4)^2 + 15q^6(a_1 - a_4)^2 + q^2((747 + 80s^2)a_1^2 + 80s^2(a_2 + a_3 - a_4)^2 + \\
& 747a_4^2 - 2a_1(80s^2(a_2 + a_3 - a_4) + 747a_4)))/(30q^2(q - s)^2 s^2(q + s)^2), \\
& s = \sqrt{\frac{3}{7} + \frac{2}{7}\sqrt{\frac{6}{5}}}, q = \sqrt{\frac{3}{7} - \frac{2}{7}\sqrt{\frac{6}{5}}}.
\end{aligned}
$$

References

[1] Kelly Black. Spectral element approximation of convection-diffusion type problems. *Applied Numerical Mathematics*, 33(1):373 − 379, 2000.

[2] Patrick Rasetarinera and M. Y. Hussaini. An efficient implicit discontinuous spectral Galerkin method. *Journal of Computational Physics*, 172(2):718–738, 2001.

[3] Stefan Fechter, Claus-Dieter Munz, Christian Rohde, and Christoph Zeiler. A sharp interface method for compressible liquid-vapor flow with phase transition and surface tension. *Journal of Computational Physics*, 336:347 − 374, 2017.

[4] Andrea D Beck, Thomas Bolemann, David Flad, Hannes Frank, Gregor J Gassner, Florian Hindenlang, and Claus-Dieter Munz. High-order discontinuous Galerkin spectral element methods for transitional and turbulent flow simulations. *International Journal for Numerical Methods in Fluids*, 76(8):522–548, 2015.

[5] David Flad, Andrea Beck, and Claus Dieter Munz. Simulation of underresolved turbulent flows by adaptive filtering using the high order discontinuous Galerkin spectral element method. *Journal of Computational Physics*, 313:1–12, 2016.

[6] Timothy Barth and Dennis Jespersen. The design and application of upwind schemes on unstructured meshes. *Aiaa Aerospace Sciences Meeting*, 0366(13), 1989.

[7] V. Venkatakrishnan. Convergence to steady state solutions of the Euler equations on unstructured grids with limiters. *Journal of Computational Physics*, 118(118):120–130, 1995.

[8] Hong Luo, Joseph D. Baum, and Rainald Löhner. On the computation of steady-state compressible flows using a discontinuous Galerkin method. *International Journal for Numerical Methods in Engineering*, 73(5):597–623, 2008.

[9] Bernardo Cockburn and Chi Wang Shu. Runge-Kutta discontinuous Galerkin methods for convection-dominated problems. *Journal of Scientific Computing*, 16(3):173–261, 2001.

[10] Guosheng Fu and Chi Wang Shu. A new troubled-cell indicator for discontinuous Galerkin methods for hyperbolic conservation laws. *Journal of Computational Physics*, 347, 2017.

[11] S Clain, S Diot, and R Loubère. A high-order finite volume method for systems of conservation laws-multi-dimensional optimal order detection (MOOD). *Journal of Computational Physics*, 230(10):4028–4050, 2011.

[12] M Dumbser and R Loubére. A simple robust and accurate a posteriori sub-cell finite volume limiter for the discontinuous Galerkin method on unstructured meshes. *J. Comput. Phys.*, 319:163–199, 2016.

[13] Matthias Sonntag and Claus-Dieter Munz. Efficient parallelization of a shock capturing for discontinuous Galerkin methods using finite volume sub-cells. *Journal of Scientific Computing*, 70(3):1–28, 2016.

[14] J Zhu, JX Qiu, C-W Shu, and M Dumbser. Runge-Kutta discontinuous Galerkin method using WENO limiters II: Unstructured meshes. *J. Comput. Phys.*, 227:4330–4353, 2008.

[15] J Zhu and JX Qiu. Hermite WENO schemes and their application as limiters for Runge-Kutta discontinuous Galerkin method III: Unstructured meshes. *J. Sci. Comput.*, 39:293–321, 2009.

[16] Wanai Li and Yu-Xin Ren. The multi-dimensional limiters for discontinuous Galerkin method on unstructured grids. *Computers & Fluids*, 96(11):368–376, 2014.

[17] Wanai Li, Jianhua Pan, and Yu-Xin Ren. The discontinuous Galerkin spectral element methods for compressible flows on two-dimensional mixed grids. *Journal of Computational Physics*, 364:314 − 346, 2018.

[18] P.L Roe. Approximate riemann solvers, parameter vectors, and difference schemes. *Journal of Computational Physics*, 43(2):357 − 372, 1981.

[19] Amiram Harten, Peter D. Lax, and Bram Van Leer. On upstream differencing and Godunov-type schemes for hyperbolic conservation laws. pages 35–61, 1997.

[20] Guang-Shan Jiang and Chi-Wang Shu. Efficient implementation of weighted eno schemes. *Journal of Computational Physics*, 126(1):202 − 228, 1996.

[21] Chi-Wang Shu and Stanley Osher. Efficient implementation of essentially non-oscillatory shock-capturing schemes, ii. *Journal of Computational Physics*, 83(1):32 − 78, 1989.

[22] Peter D Lax. Weak solutions of nonlinear hyperbolic equations and their numerical computation. *Communications on Pure and Applied Mathematics*, 7(1):159–193, 1954.

[23] L. Krivodonova, J. Xin, J.-F. Remacle, N. Chevaugeon, and J.E. Flaherty. Shock detection and limiting with discontinuous Galerkin methods for hyperbolic conservation laws. *Applied Numerical Mathematics*, 48(3):323 − 338, 2004. Workshop on Innovative Time Integrators for PDEs.

[24] Paul Woodward and Phillip Colella. The numerical simulation of two-dimensional fluid flow with strong shocks. *Journal of Computational Physics*, 54(1):115–173, 1984.

[25] Jun Zhu, Jianxian Qiu, Chi Wang Shu, and Michael Dumbser. Runge-kutta discontinuous Galerkin method using WENO limiters ii. *Journal of Computational Physics*, 227(9):4330–4353, 2008.

[26] Oliver Kolb. On the full and global accuracy of a compact third order WENO scheme. *Siam Journal on Numerical Analysis*, 52:2335–2355, 2014.

[27] Wanai Li and Yu-Xin Ren. A multidimensional limiting procedure for the discontinuous Galerkin method. *Computers&Fluids*, 54(3):695–706, 2014.

[28] Changqing Hu and Chi Wang Shu. Weighted essentially non-oscillatory schemes on triangular meshes. *Journal of Computational Physics*, 150(1):97–127, 1999.

[29] Peter D. Lax and Xu Dong Liu. Solution of two-dimensional Riemann problems of gas dynamics by positive schemes. 192:319–340, 1998.

[30] James J. Quirk. A contribution to the great Riemann solver debate. *International Journal for Numerical Methods in Fluids*, 18(6):555 − 574, 1994.